Heat transfer and fluid flow analysis of a 4 kW solar thermochemical reactor for ceria redox cycling

Journal Article

Author(s):
Furler, Philipp; Steinfeld, Aldo
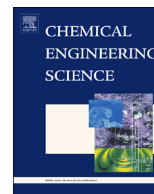
Heat transfer and fluid flow analysis of a 4 kW solar thermochemical reactor for ceria redox cycling

Philipp Furler, Aldo Steinfeld *

Department of Mechanical and Process Engineering, ETH Zurich, 8092 Zurich, Switzerland

ARTICLE INFO

ABSTRACT

A solar reactor consisting of a cavity-receiver containing a reticulated porous ceramic (RPC) foam made of CeO_2 is considered for effecting the splitting of H_2O and CO_2 via a thermochemical redox cycle. A transient 3D heat and mass transfer model of the reduction step is formulated and solved using Monte-Carlo ray-tracing coupled to computational fluid dynamics. Experimental validation is accomplished in terms of measured temperatures and O_2 evolution rates obtained with a solar reactor prototype tested under high-flux radiative power inputs in the range 2.8–3.8 kW and mean solar concentration ratios up to 3024 suns. Critical temperatures of up to 2250 K induced CeO_2 sublimation, which in turn affected detrimentally the solar reactor performance. The model is applied to analyze an improved geometrical design with alternative flow configuration, enabling more uniform radiative absorption and temperature distributions, and resulting in a higher solar-to-fuel energy conversion efficiency.

1. Introduction

Solar thermochemical cycles based on metal oxide redox reactions can split CO_2 and H_2O to produce a mixture of CO and H_2 (syngas), which can be further processed to liquid hydrocarbon fuels (Steinfeld, 2005; Perkins and Weimer, 2004; Smestad and Steinfeld, 2012; Miller et al., 2013). Non-stoichiometric cerium oxide has emerged as an attractive redox active material because of its relatively high oxygen solid-state conductivity, contributing to fast redox kinetics (Chueh et al., 2012) and because of its crystallographic stability over a wide range of oxidation states (Chueh and Haile, 2010; Zinkevich et al., 2006). The two-step H_2O/CO_2-splitting solar thermochemical cycle based on oxygen-

deficient ceria is represented by

High–temparature reduction :
$$CeO_2 \overset{+\Delta H}{\Rightarrow} CeO_{2-\delta} + \frac{\delta}{2}O_2 \tag{1}$$

Low–temperature oxidation with H_2O
$$: \quad CeO_{2-\delta} + \delta H_2O \overset{-\Delta H}{\Rightarrow} CeO_2 + \delta H_2 \tag{2a}$$

Low–temperature oxidation with CO_2
$$: \quad CeO_{2-\delta} + \delta CO_2 \overset{-\Delta H}{\Rightarrow} CeO_2 + \delta CO \tag{2b}$$

In the first, high-temperature endothermic step, ceria is thermally reduced to a non-stoichiometric state using concentrated solar energy. In the subsequent, lower temperature exothermic step, ceria is re-oxidized with H_2O and/or CO_2 to produce H_2 and/or CO, respectively. Solar reactors for effecting this cycle include cavity-receivers with rotating or stationary structures, (Lapp et al., 2013;

Diver et al., 2008; Kaneko et al., 2007) glass dome reactors, (Abanades and Flamant, 2006) aerosol flow reactors, (Scheffe et al., 2014) and moving and fluidized bed reactors (Ermanoski et al., 2013; Kodama et al., 2008). We have developed a solar reactor that features a cavity-receiver containing porous ceria and demonstrated experimentally the production of H_2 from H_2O (Chueh et al., 2010) and CO from CO_2, (Chueh et al., 2010; Furler et al., 2012; Furler et al., 2014) as well as the co-production of H_2 and CO by simultaneous splitting a mixture of H_2O and CO_2 using the solar cavity-receiver reactor (Furler et al., 2012).

In this work, we present a transient 3D heat and mass transfer model of the solar reactor for performing the high-temperature solar reduction step (Eq. (1)). The model couples Monte-Carlo (MC) ray-tracing and computational fluid dynamics (CFD) techniques. Validation is accomplished by comparing numerically calculated and experimentally measured temperatures, O_2-evolutions, and solar-to-fuel energy conversion efficiencies obtained with the 4-kW solar reactor prototype. The validated model is further applied to examine an improved geometrical design with alternative flow configuration and to identify the major sources of energy loss as well as strategies to minimize them.

2. Solar reactor configuration and experimental setup

The solar reactor configuration is shown schematically in Fig. 1(a). The engineering design has been presented previously in detail (Furler et al., 2012). The main features are briefly summarized here. The solar reactor consisted of a cavity-receiver with a 4 cm dia. circular aperture for the access of concentrated solar radiation. The aperture was closed by a 24 cm dia., 3 mm thick clear fused quartz disk window mounted on a frustum. A compound parabolic concentrator (CPC) (Welford and Winston, 1989) was incorporated into the aperture to further boost the solar concentration ratio[1] to mean values of up to 3024 suns. The cavity contained a cylinder of reticulated porous ceramic (RPC) foam made of pure ceria composed of four 20 mm-tick, 60 mm-i.d., 100 mm-o.d. rings, and a single 20 mm-thick, 100 mm-o.d. disk. The total mass of the CeO_2 cylinder was 1413 g. The cavity was insulated by a 10 mm-thick layer of CeO_2 laminate surrounded by Al_2O_3–SiO_2 and sheathed by an outer shell made of Inconel 600. An annular gap between RPC and insulation induced uniform radial flow across the RPC cylinder. Temperatures were measured at the outer surface of the RPC (B-type thermocouples), in the middle of the Al_2O_3–SiO_2 insulation, and at the outer Inconel wall (K-type thermocouples). Argon (99.999% purity) flow rates were regulated by electronic mass flow controllers (Bronkhorst F-201C) and injected through four radial inlet ports and one axial nozzle located at the frustum close to the quartz window. Gases exited the reactor through an axial outlet port at the rear plate. The gas composition was monitored at the outlet by gas chromatography (Varian 490), supplemented by a paramagnetic alternating pressure based O_2 detector (Siemens Oxymat 6). Experimentation was performed at the ETH's high flux solar simulator (HFSS): an array of seven Xe arc lamps, close-coupled to truncated ellipsoidal reflectors, provided an external source of intense thermal radiation (mostly in the visible and IR spectra) that closely approximated the heat transfer characteristics of highly concentrating solar systems, such as solar towers and dishes (Petrasch et al., 2007). The radiative flux distribution at the aperture plane was measured optically using a calibrated CCD camera focused on a water-cooled, Al_2O_3-plasma coated Lambertian (diffusely

reflecting) target. The radiative power input through the aperture P_{solar} was obtained by integration of the radiative flux and verified with measurements using a water-calorimeter.

A typical experimental run consisted of two consecutive stages: (1) the solar reactor was pre-heated for 30 min at a radiative power input $P_{solar}=0.8$ kW; (2) the radiative power input was increased to 2.8, 3.4, or 3.8 kW to initiate thermal reduction. The corresponding mean solar concentration ratios over the aperture were 2228, 2706, and 3024. During both stages, the Ar flow rate was kept constant at 1.8 L min^{-1} (SLPM; mass flow rate calculated at 273.15 K and 101.325 Pa) through the side inlets (uniformly distributed over the four radial inlets) and 0.2 L min^{-1} through the reactor front.

3. Heat and mass transfer analysis

Fig. 1(b) shows a schematic representation of the individual computational domains (fluid, solid, and porous) of the model. The reactor cavity, reactor front, gas-gap, inlets, and outlet are modeled as fluid domains, assumed to be a non-participating media for radiation. Laminar flow conditions ($Re \ll 150$ in all domains, (Seguin et al., 1998)) and ideal gas mixtures are assumed. The Al_2O_3–SiO_2 insulation, ceria laminate, and the inconel reactor shell are modeled as solid domains. The reactive ceria RPC is modeled as a homogeneous and radiative participating two-phase porous domain.

Governing equations − The continuity, species conservation, momentum, and energy conservation equations in the fluid domains are given respectively by

$$\frac{\partial \rho}{\partial t} + \nabla \cdot (\rho \overline{U}) = 0 \tag{3}$$

$$\frac{\partial (\rho Y_{O_2})}{\partial t} + \nabla(\rho \overline{U} Y_{O_2}) = 0 \tag{4}$$

$$\frac{\partial}{\partial t}(\rho \overline{U}) + \nabla \cdot (\rho \overline{UU}) = -\nabla p + \nabla \cdot \mu \left(\nabla \overline{U} + (\nabla \overline{U})^{\mathrm{T}} - \frac{2}{3}\overline{\overline{I}} \nabla \cdot \overline{U} \right) + \overline{S}_{M,\text{buoy}} \tag{5}$$

$$\frac{\partial}{\partial t}(\rho h) + \nabla \cdot (\overline{U} \rho h) = \nabla \cdot (k \nabla T) \tag{6}$$

where ρ is the density, $\overline{U}$ is the velocity vector, Y_{O_2} the concentration of O_2 in the gas mixture, μ is the dynamic viscosity, $\overline{\overline{I}}$ is the identity matrix, $\overline{S}_{M,\text{buoy}}$ is an external momentum source accounting for buoyancy, h is the enthalpy, and, k is the thermal conductivity of the gas mixture. Gas diffusion is neglected in Eqs. (4) and (6) because $Pe_{\text{mass}} > 1$, thus advective mass transport is dominant compared to mass diffusion. Gas flows are modeled as Ar–O_2 mixtures of variable composition, determined by solving Eq. (4). Kinetic energy and viscous dissipation are neglected in Eq. (6) because $U \ll 1$ m s^{-1} and $Br \ll 1$.

Due to the absence of flows, the energy conservation equation in the solid domains is simplified to

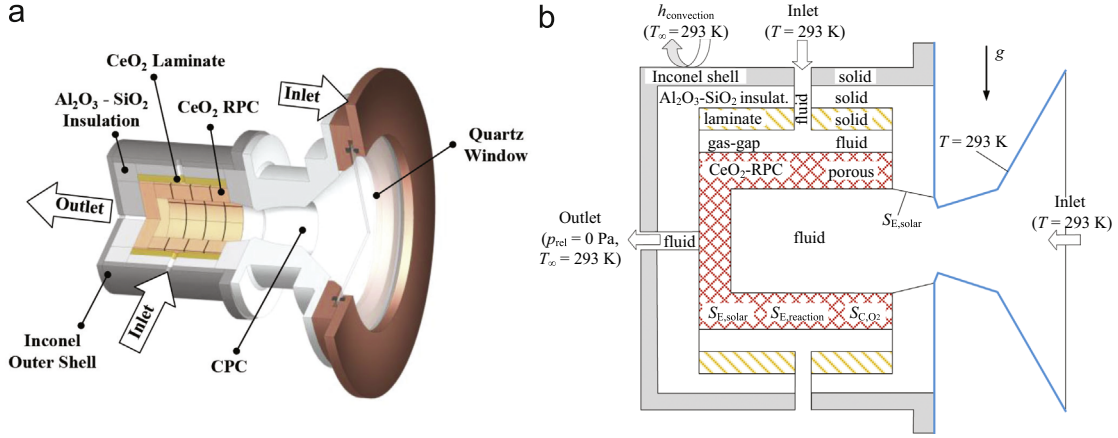$$\frac{\partial (\rho h)}{\partial t} = \nabla \cdot (k \nabla T) \tag{7}$$

The governing equations for the fluid phase of the RPC porous domain are as follows:

$$\frac{\partial \rho \varepsilon}{\partial t} + \nabla \cdot (\rho \overline{\overline{K}} \cdot \overline{U}) = S_{C,O_2} \tag{8}$$

$$\frac{\partial (\rho \varepsilon Y_{O_2})}{\partial t} + \nabla(\rho \overline{\overline{K}} \cdot \overline{U} Y_{O_2}) = S_{C,O_2} \tag{9}$$

$$\frac{\partial (\varepsilon \rho \overline{U})}{\partial t} + \nabla \cdot \left(\rho \left(\overline{\overline{K}} \cdot \overline{U} \right) \overline{U} \right) = -\nabla p +$$
$$\nabla \cdot \left(\mu \overline{\overline{K}} \cdot \left(\nabla \overline{U} + (\nabla U)^{\mathrm{T}} - \frac{2}{3}\overline{\overline{I}} \nabla \cdot \overline{U} \right) \right) + \overline{S}_{M,\text{buoy}} + \overline{S}_{M,\text{porous}} \tag{10}$$

---

[1] The solar concentration ratio, C, is defined as solar radiative power intercepted by the aperture. C is expressed in units of "suns" when normalized to 1 kW m^{-2}.

Fig. 1. (a) Schematic of the solar reactor configuration and (b) schematic of the fluid, solid, and porous domains. Also indicated are the boundary conditions and source terms.

$$\frac{\partial(\varepsilon\rho h)}{\partial t} + \nabla \cdot \left(\rho\overline{\overline{K}} \cdot \overline{U}h \right) = \nabla \cdot (k\nabla T) + S_{E,\text{solar}} + \nabla q_r + Q_{fs} \tag{11}$$

where ε is the volume porosity, $\overline{\overline{K}}$ is the isotropic porosity tensor, S_{C,O_2} the O_2 mass source accounting for oxygen evolution during thermal reduction, $\overline{S}_{M,\text{porous}}$ a momentum source accounting for viscous losses and inertial drag forces imposed by the porous structure on the fluid according to the Dupuit–Forchheimer law, $S_{E,\text{solar}}$ accounts for incoming absorbed solar radiation from the HFSS, and ∇q_r is the radiative source term accounting for radiation exchange. The energy conservation equations of fluid and solid are coupled via the source term $Q_{fs} = h_{fs} \cdot A_{fs}(T_s - T_f)$, where h_{fs} is the interphaseal heat transfer coefficient, A_{fs} is the fluid–solid area density, and T_s and T_f are the temperatures of the solid and fluid, respectively. Thermal equilibrium between both phases ($T_s = T_f$) is enforced by setting h_{fs} artificially high (10,000 W m^{-1} K^{-1}), which is reasonable in this case, as $Pe_{th} < 1$, thus thermal diffusion is dominant over advection.

The governing equation for the solid phase of the RPC porous domain is:

$$\frac{\partial((1-\varepsilon)\rho h)}{\partial t} = \nabla \left(k\overline{\overline{K_s}} \cdot \nabla T \right) + S_{E,\text{reaction}} + Q_{sf} \tag{12}$$

where $S_{E,\text{reaction}}$ is the energy sink accounting for the endothermicity of the CeO_2 reduction reaction.

The RPC is modeled as participating media. The radiative transfer equation for an isotropic, gray, absorbing-emitting-scattering participating media is given by

$$\frac{dI(\overline{r},\overline{s})}{ds} = -\beta I(\overline{r},\overline{s}) + \alpha I_b(\overline{r}) + \frac{\sigma}{4\pi}\int_{4\pi} I(\overline{r},\overline{s}')d\omega' \tag{13}$$

where $\overline{r}$ is the position vector, $\overline{s}$ is the direction vector, s is the path length, β, α and σ are the extinction, absorption, and scattering coefficients, respectively, I is the radiation intensity depending on position r and direction s, I_b is the blackbody radiation intensity depending on the local temperature T, and ω is the solid angle. The radiation source term in Eq. (11) is given by

$$\nabla q_r = \alpha \left(4\pi I_b - \int_{4\pi} I d\omega \right) \tag{14}$$

Material properties—Material properties are listed in Table 1. Heat capacities (c_p) of CeO_2 and Al_2O_3–SiO_2 insulation have been measured by differential scanning calorimetry (DSC) using a Netsch DSC 404 C Pegasus in the temperature range 470–1100 K and 470–1400 K, respectively. The thermal conductivity (k) of CeO_2 laminate was measured in the temperature range of 300–973 K by laser flash analysis using a Netsch Laserflash-analyser LFA 457. The thermal conductivity of the Al_2O_3–SiO_2 insulation was taken from the manufacturer (Zircar Zirconia, Inc., 2014). The effective heat and mass

transfer properties of the RPC structure have been determined by direct numerical pore-level simulation on the exact RPC geometry obtained by computer tomography (Suter et al., 2014; Haussener et al., 2010; Petrasch et al., 2008). The effective extinction coeffcient of the RPC was determined by pore-level MC on its 3-D tomographic scans (Suter et al., 2014; Haussener et al., 2010). The scattering and absorption coefficients were calculated from $\sigma = \rho_s \cdot \beta$ and $\alpha = (1 - \rho_s) \cdot \beta$, where ρ_s is the surface total reflectance weighted by the Planck blackbody spectral emission in a temperature range 300–2500 K. ρ_s of partially reduced ceria at $\delta = 0.035$ was measured with an integrating sphere using a monochromatic collimated beam of light emitted by a Xe-arc in a spectral range 300–1600 nm under three different incident angles (8°, 40°, and 60°). The thermal conductivity of CeO_2, the optical properties of the Al_2O_3–SiO_2 insulation, polished aluminum frustum and CPC were taken from the literature (Touloukian and Dewitt, 1972; Touloukian, 1967; Siegel and Howell, 2002). The quartz window is modeled as a partially transparent thin disc with τ_s of 0.94 and ρ_s of 0.06.

Boundary conditions and source terms—The boundary conditions and source terms are schematically indicated in Fig. 1(b). The radiative power input delivered by the HFSS and absorbed within the cavity-receiver was determined by MC ray tracing, yielding the energy sources $S_{E,\text{solar}}$ to the CFD code. At the outer reactor shell, natural convective heat transfer was modeled using Nusselt correlations for vertical flat surfaces (Churchill and Chu, 1975) and for horizontal cylinders (Churchill and Chu, 1975). The water-cooled CPC and frustum were assumed to be at 293 K. 0.45 L min^{-1} of Ar containing an O_2 mass fraction of 1×10^{-5} was injected at $T = 293$ K normally to the inlet surface through each of the four radial inlet ports. 0.2 L min^{-1} of Ar flow with $P_{O_2} = 1 \times 10^{-5}$ atm was injected at $T = 293$ K axially and uniformly distributed over the window surface. A the outlet, $p_{\text{relative}} = 0$ Pa. The reduction of nonstoichiometric ceria was modeled based on thermodynamic equilibrium, as previous work has shown that the overall kinetics were controlled by heat transfer (Furler et al., 2012). Experimental data by Panlener et al. (1975) was fitted according to the procedure described by Scheffe and Steinfeld (2012) and Ermanoski et al. (2013) yielding the following expressions of nonstoichiometry δ and reaction enthalpy ΔH as a function of temperature and P_{O_2}:

$$\log(\delta) = a_1 + a_2 \cdot \log(P_{O_2}/P_0) + a_3 \cdot \log(P_{O_2}/P_0)^2 + a_4 \cdot \log(P_{O_2}/P_0)^3$$
$$+ a_5 \cdot T + a_6 \cdot \log(P_{O_2}/P_0) \cdot T + a_7 \cdot \log(P_{O_2}/P_0)^2 \cdot T + a_8 \cdot \log(P_{O_2}/P_0) \cdot T^2 \tag{15}$$

$$\Delta H = b_1 + b_2 \cdot \delta^{0.5} \tag{16}$$

The fitting parameters are listed in Table 2.

Table 1
Material properties used in the CFD analysis.

		T (K)	Ref.
CeO₂ RPC			
Density (kg m^{-3})	7220	–	
Porosity (%)	63	–	
Total CeO₂ mass (g)	1413	–	Furler et al., 2012
Permeability (m²)	4.63376×10^{-8}	–	Suter et al., 2014
Dupuit–Forchheimer coefficient (m^{-1})	1616.7	–	Suter et al., 2014
Thermal conductivity $_{solid}$ (W m^{-1} K^{-1})	$(17.8004 - 0.02402 \times T + 0.0000112032$ $\times T^2 - 1.7 \times 10^{-9} \times T^3)/$ $(7.9799 + 0.00483384 \times T - 9.3397 \times 10^{-6}$ $\times T^2 + 2.8 \times 10^{-9} \times T^3)$	280–2000K	Suter et al., 2014; Touloukian, 1967
	0.4	> 2000K	
Specific heat capacity (J kg^{-1} K^{-1})	$-0.0001271 \times T^2 + 0.2697656 \times T + 299.8695684$	280–1100K	
	444.27	> 1100K	
Extinction coefficient (m^{-1})	497.8	–	Suter et al., 2014
Surface reflectance (at $\delta = 0.035$)	$-3 \times 10^{-5} \times T + 0.2866$	300–2500	
Absorption coefficient CeO$_{1.965}$ (m^{-1})	$(1 - (-0.00006 \times T + 0.411)) \times 497.8$	300–2500	
Scattering coefficient CeO$_{1.965}$ (m^{-1})	$(-0.00006 \times T + 0.411) \times 497.8$	300–2500	
Fluid–solid heat transfer coefficient (W m^{-2} K^{-1})	10000		
Fluid–solid area density (m^{-1})	952	–	Suter et al., 2014
Al₂O₃–SiO₂ insulation			
Density (kg m^{-3})	560.65	–	Zircar Zirconia, 2014
Specific heat capacity (J kg^{-1} K^{-1})	$4 \times 10^{-7} \times T^3 - 1.3797 \times 10^{-3} \times T^2 + 1.5987289$ $\times T + 477.6995948$	≤ 1480K	
	1118.44	> 1480K	
Thermal conductivity (W m^{-1} K^{-1})	$0.00012926 \times T + 0.019654$	280–2200	Zircar Zirconia, Inc., 2014
Hemispherical total emittance	0.28	–	Touloukian and Dewitt, 1972
CeO₂ laminate			
Density (kg m^{-3})	504.4	–	
Specific heat capacity (J kg^{-1} K^{-1})	$-0.0001271 \times T^2 + 0.2697656 \times T + 299.8695684$	280–1100K	
	444.27	> 1100K	
Thermal conductivity (W m^{-1} K^{-1})	$2.2 \times 10^{-7} \times T^2 - 2.8387 \times 10^{-4} \times T + 0.17678688$	295–2000	
Hemispherical total emittance	0.7	–	
Inconel 600			
Density (kg m^{-3})	8470		Special Metal Corporation, 2014
Specific heat capacity (J kg^{-1} K^{-1})	$0.2827 \times T + 327.29$	123–1173	Special Metal Corporation, 2014
Thermal conductivity (W m^{-1} K^{-1})	$0.0158 \times T + 10.169$	123–1073	Special Metal Corporation, 2014
Argon			
Thermal conductivity (W m^{-1} K^{-1})	$2.35332617 \times 10^{-12} \times T^3 - 1.289997670118 \times 10^{-8}$ $\times T^2 + 4.837061371854420 \times 10^{-5} \times T$ $+ 0.00483418574527758$	290–2400	Zimmermann, 2012
Dynamic viscosity (kg m^{-1} s^{-1})	$3.51928 \times 10^{-15} \times T^3 - 2.0456156372 \times 10^{-11}$ $\times T^2 + 6.84961187335571 \times 10^{-8}$ $\times T + 4.20667800364964 \times 10^{-6}$	290–2400	Zimmermann, 2012

Numerical Solution—The MC simulations were performed using the in-house code VEGAS (Petrasch, 2010) with 10^{10} rays. The CFD simulations were performed with ANSYS CFX 14.0. The discrete transfer radiation model was applied to solve Eq. (13), (Lockwod and Shah, 1981; Ansys Inc., 2012) which was transformed into a set of transport equations for I and solved for discrete solid angles along s. The governing equations are discretized both in space (284,411–3,277,176 tetrahedras) and time (time step=2 s) and solved on the individual control volumes by the finite-volume method with a first order upwind and second order backward Euler scheme. Simulations were performed on the central high-performance cluster Brutus of ETH Zurich.

4. Experimental validation

The MC simulation of the HFSS was experimentally validated with measurements of the radiative flux distribution at the focal plane. Fig. 2 shows the radiative flux distribution for all seven Xe-arcs of the HFSS: (a) measured with a calibrated CCD camera on a Lambertian

target; (b) simulated by MC, and (c) measured and simulated along the vertical and horizontal axes. The mean relative difference between the measured and simulated values over the aperture size was 2.9% with a standard deviation of 0.045 MW m^{-2}. Deviations are attributed to non-ideal ellipsoidal geometry and misalignment.

Experimental validation of the solar reactor model was accomplished by comparing its numerical outputs to experimental data obtained with the prototype solar reactor tested at the HFSS for a set of three experimental runs with $P_{solar} = 2.8$, 3,4, and 3.8 kW. A summary of the operating conditions is presented in Table 3 (Furler et al., 2012). Fig. 3(a)–(c) shows the experimentally measured (dashed curves) and numerically calculated (solid curves) temperatures at locations $T_{B,1}$, $T_{B,2}$, $T_{K,1}$, $T_{K,2}$, and $T_{K,3}$ (positions indicated in Fig. 4) as a function of time for three runs with $P_{solar} = 2.8$, 3.4, and 3.8 kW. Also shown are the measured (dashed curves) and simulated (solid curve) O₂ evolution curves at the outlet of the reactor as a function of time. The temperature of the ceria RPC rose rapidly with increasing P_{solar}, from the initial 1015 K (average of $T_{B,1}$ and $T_{B,2}$) after pre-heating at 0.8 kW to 1800 K at 2.8 kW, 1855 K at 3.4 kW, and 1899 K at 3.8 kW. Additionally,

Table 2
Fitting parameters for δ and ΔH.

Fitting parameter	Value	Fitting parameter	Value
a_1	-9.783687979325373	a_7	0.000009111263871567086
a_2	0.43818838204603383	a_8	$3.04372591882286 \times 10^{-7}$
a_3	-0.017553628274187237	b_1	969.4087154075294
a_4	-0.00040499337269384977	b_2	-503.7387449398726
a_5	0.004301105768218843		
a_6	-0.0008944789208869576		
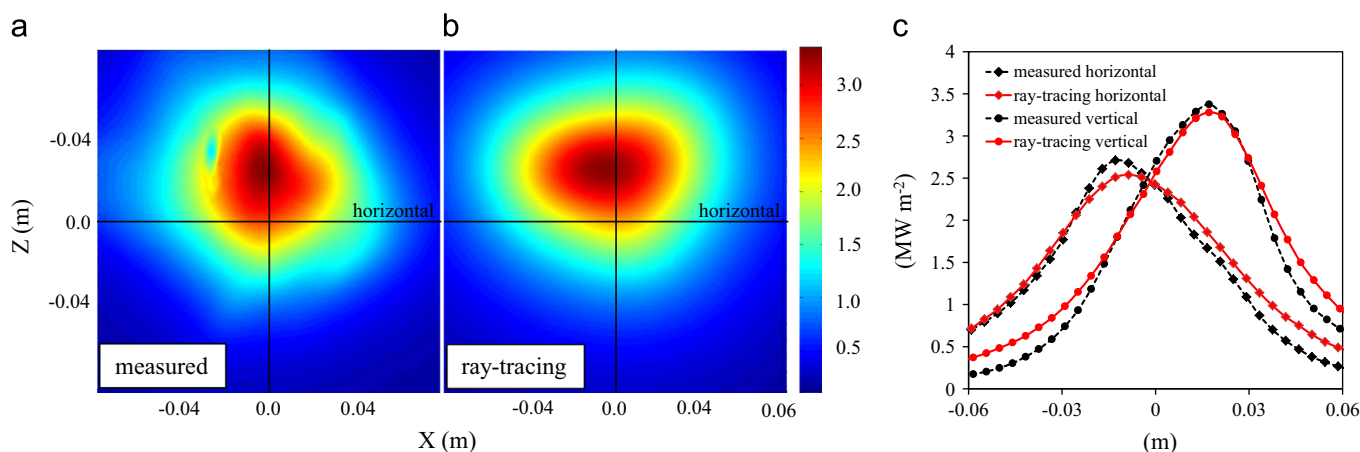
Fig. 2. Radiative flux distribution of the ETH's HFSS (7 Xe-arc lamps): (a) measured with a calibrated CCD camera; (b) simulated by MC, and (c) measured and simulated along the vertical and horizontal planes.

Table 3
Operating conditions used during the experimental campaign and applied for the model validation.

Power input during reduction, P_{solar}, (kW)	2.8	3.4	3.8
Duration of pre-heating (min)	30	30	30
Power input during pre-heating (kW)	0.8	0.8	0.8
Duration of reduction step (min)	22	18	16
Ar flow rate front (L min^{-1})	0.2	0.2	0.2
Ar flow rate radial inlets (L min^{-1})	1.8	1.8	1.8
CeO$_2$ mass loading (g)	1413	1413	1413

as P_{solar} increased from 2.8 to 3.8 kW, both the peak and average heating rates increased from 127 K min^{-1}/36 K min^{-1} to 163 K min^{-1}/56 K min^{-1}. As expected, higher heating rates and temperatures lead to higher O$_2$ peak rates and higher total O$_2$ evolution. This trend is captured by the reactor model which predicts a peak temperature (average of $T_{B,1}$ and $T_{B,2}$) and a total O$_2$ evolution of 1793 K and 1.33 ml g^{-1} CeO$_2$ for 2.8 kW, 1837 K and 1.73 ml g^{-1} CeO$_2$ for 3.4 kW, and 1869 K And 1.93 ml g^{-1} CeO$_2$ for 3.8 kW, respectively. The temperature agreement between simulation and experiment is reasonably good at all locations for the three runs. Discrepancies are attributed to uncertainties in the positioning of the thermocouples and to the extrapolation of measured material properties to higher temperatures, such as the case for k of CeO$_2$ laminate and Al$_2$O$_3$–SiO$_2$ insulation. Good matching is also obtained between measured and simulated O$_2$ evolution rates, especially in the cases of 2.8 kW and 3.4 kW, considering the uncertainties with thermodynamic data at above 1773 K.

The solar-to-fuel energy conversion efficiency is defined as follows:

$$\eta_{solar-to-fuel} = \frac{\Delta H_{fuel} \int r_{fuel} dt}{\int P_{solar} \, dt + E_{inert} \int r_{inert} \, dt} \tag{17}$$

where r_{fuel} is the molar rate of fuel production, ΔH_{fuel} is the heating value of the fuel, P_{solar} is the solar radiative power input, r_{inert} is the flow rate of the inert gas, and E_{inert} is the energy required to separate the inert gas (assumed 20 kJ mol^{-1} inert gas) (Haering 2008). Assuming stoichiometric fuel production ($r_{fuel} = 2r_{O_2}$) according to Eq. (2b) and accounting for 15 min of pre-heating, the experimentally determined values of efficiency were: $\eta_{solar-to-fuel} = 1.16\%$, 1.42%, and 1.73% for 2.8 kW, 3.4 kW, and 3.8 kW, respectively. These are slightly higher than the numerically simulated values: $\eta_{solar-to-fuel} = 1.06\%$, 1.39%, and 1.55% for 2.8 kW, 3.4 kW, and 3.8 kW, respectively, attributed to the slight under-prediction of the total O$_2$ yield. Note that the sensible heat of solids and gases was not recovered during the experimental runs.

5. Modelling results and discussion

Incoming thermal radiation—Fig. 5 shows the radiative flux distribution at $P_{solar} = 3.8$ kW that is: (a) impinging on the exposed ceria RPC surface; (b) absorbed on the exposed top Al$_2$O$_3$–SiO$_2$ insulation; and (c) absorbed on the water-cooled cooper-ring (part of reactor front), as determined by MC. Both axial and radial non-uniformity is observed. The front parts of the RPC and the Al$_2$O$_3$–SiO$_2$ insulation are more strongly irradiated than locations towards the rear end because of the large rim angle of the HFSS ($> 45°$) combined with the optical design of the CPC (outlet angle $= 90°$) which directs the incoming radiation mostly onto areas close to the reactor front. This resulted in an average radiative flux of 122 kW m^{-2} on the RPC side walls and 250 kW m^{-2} on the RPC back plate compared to peak 690 kW m^{-2} at locations close to the reactor front. The radial non-uniformity in flux distribution is attributed to partial misalignment of the Xe-arcs. In total, 2.3 kW of radiative power (60.5% of P_{solar}) is volumetrically absorbed within the RPC structure.

The Al$_2$O$_3$–SiO$_2$ insulation receives an average and peak radiative flux of 210 and 393 kW m^{-2}, respectively, resulting in
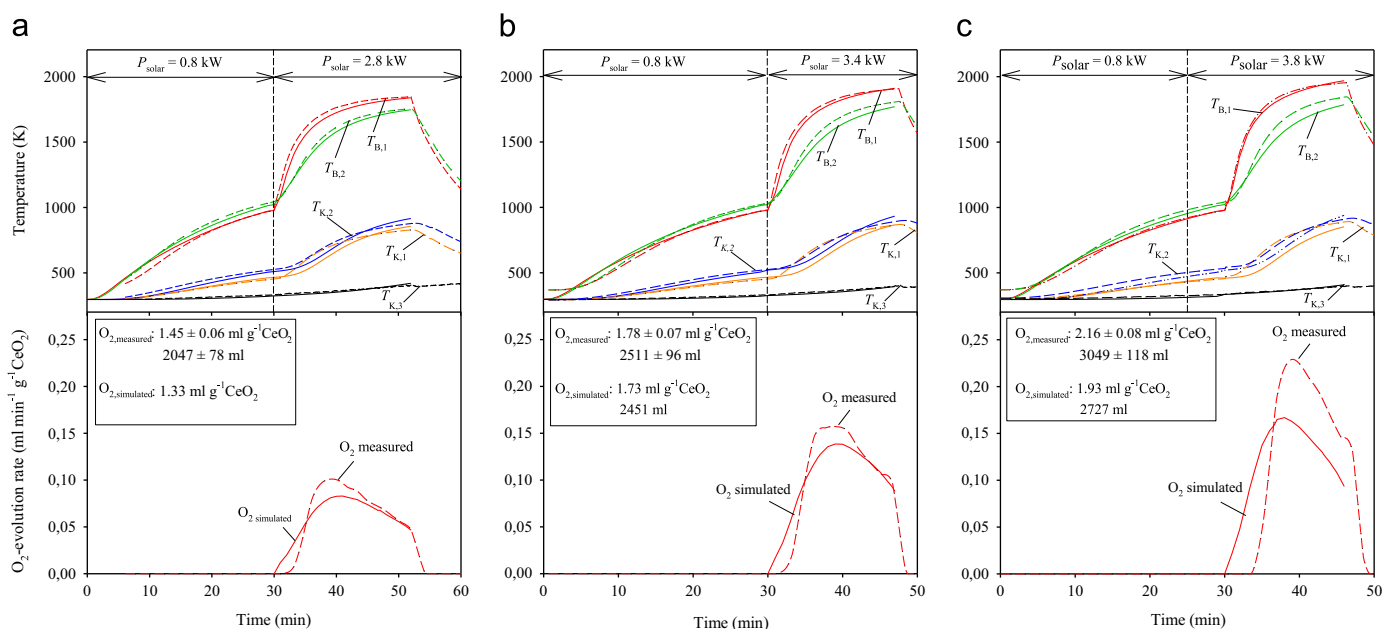
Fig. 3. (Top) Numerically calculated (solid lines) and experimentally measured (dashed lines) temperatures at locations indicated in Fig. 4 and (bottom) numerically calculated and measured O_2 evolution rate at the outlet of the reactor as a function of time for the experimental run performed at: (a) $P_{solar}=2.8$ kW, (b) $P_{solar}=3.4$ kW, and (c) $P_{solar}=3.8$ kW.
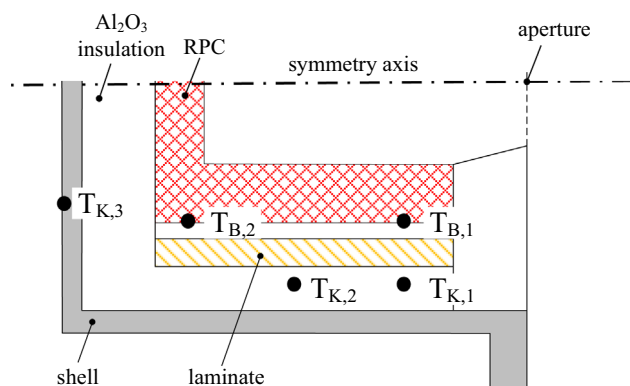
Fig. 4. Schematic cross-section of the solar reactor showing the measurement locations of the type-B and type-K thermocouples: $T_{B,1}$ and $T_{B,2}$ at the outer surface of the ceria RPC; $T_{K,1}$ and $T_{K,2}$ in the middle of the Al_2O_3–SiO_2 insulation; and $T_{K,3}$ at the outer reactor shell.

0.93 kW (24.5% of P_{solar}) absorbed radiative power. The water-cooled copper ring which is placed directly after the CPC absorbs 0.19 kW (5% of P_{solar}).

Temperature distribution and flow analysis—Fig. 6(a) shows the temperature distribution and normalized velocity vectors of the flow field in the vertical cross-section of the solar reactor after 30 min pre-heating with $P_{solar}=0.8$ kW and 16 min reduction with $P_{solar}=3.8$ kW. The O_2 concentration at peak O_2 evolution is depicted in Fig. 6(b). As expected, locations exposed to high radiative fluxes exhibit higher temperatures. The model predicts a peak and average ceria temperature of 2258 K and 1915 K, respectively. The highest temperature is achieved close to the reactor front where the RPC is exposed to a radiative flux exceeding 650 kW m^{-2}. Such high temperatures are undesired as it causes ceria sublimation and mechanical failure of the RPC structure, as experimentally observed (Furler et al., 2012; Furler et al., 2012). Due to the very high ceria temperatures, the O_2 concentration reaches a peak value of 17% at these locations. The temperature difference across the RPC is 145 K on average. For the Al_2O_3–SiO_2 insulation, the model predicts temperatures above 2200 K at certain locations close to the aperture, which exceeds the melting temperature (2143 K) as
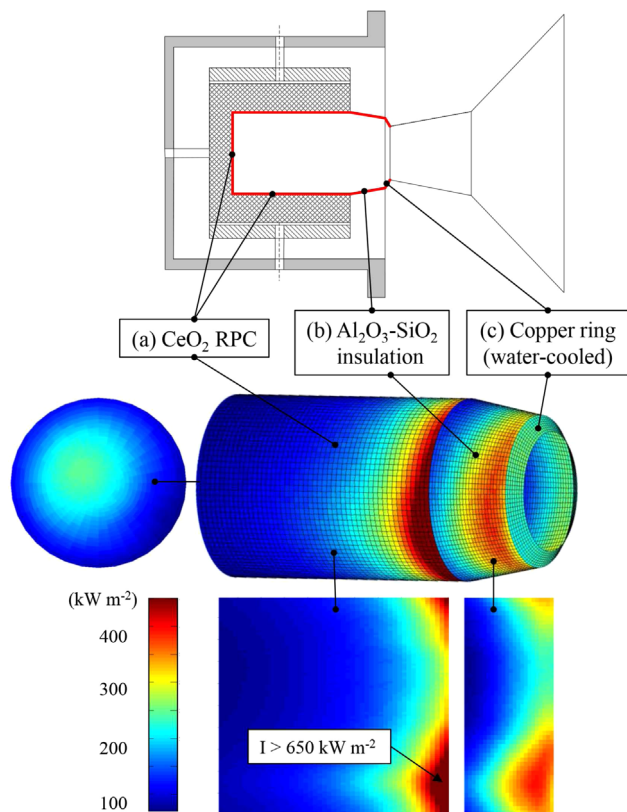
Fig. 5. Radiative heat flux at $P_{solar}=3.8$ kW: (a) impinging on the innermost exposed RPC surface, (b) absorbed by the exposed Al_2O_3–SiO_2 insulation, and (c) absorbed by the water-cooled copper ring close to the reactor's aperture.

experimentally verified. The contact surface of the Al_2O_3–SiO_2 and CeO_2 laminate is maintained below 1700 K to prevent undesired side reactions (Mizuno et al., 1975). The mean gas temperature in the cavity and at the outlet are 1798 K and 1767 K, respectively. In the reactor front, the mean gas temperature is only 488 K due to the injected flows
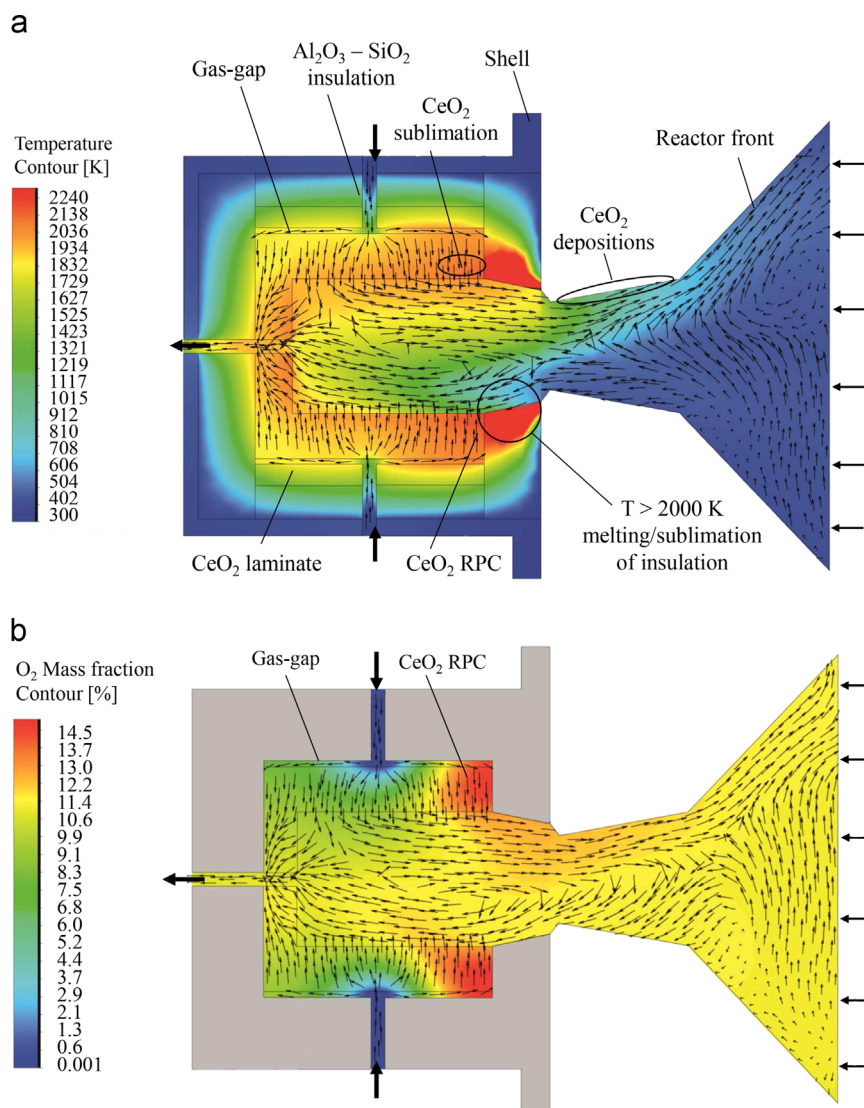
Fig. 6. (a) Normalized velocity vectors and temperature distribution in the vertical cross-section after 30 min pre-heating with $P_{solar}=0.8$ kW and 16 min reduction with $P_{solar}=3.8$ kW and (b) Normalized velocity vectors and O_2-concentration in the vertical cross-section of the cavity-receiver at peak O_2-evolution ($t=38$ min) at $P_{solar}=3.8$ kW.

at $T=293$ K and the water-cooled surfaces. Free convection is dominating the flow pattern, causing internal circulations and forcing the radially incoming gases to flow into the reactor front. This situation has a detrimental effect on $\eta_{solar-to-fuel}$ because O_2 is not efficiently purged from the reactor, limiting the ceria reduction according to Eq. (1). Furthermore, ceria vapor derived by sublimation of the overheated RPC is carried out by the gas flow and condenses on the water-cooled specular CPC, lowering its reflectivity and consequently the radiative power input through the aperture by up to 15%, as experimentally observed (Furler et al., 2012).

These gas circulations can be avoided by increasing the purge gas flow and reversing the flow direction. Fig. 7 shows a contour plot of the velocity and normalized velocity vectors of the flow field in the vertical cross section for $P_{solar}=2.8$ kW and an Ar flow rate of 12.5 L min^{-1} provided tangentially through 6 nozzles around the window circumference. The flow direction is reversed by operating the radial openings as additional outlets instead of inlets. For simplicity, the reduction chemistry is omitted. The tangential injection of Ar causes a swirl flow pattern preventing back flow of gases from the cavity into the reactor front, thus

depositions of sublimated CeO_2 at the CPC surface. In contrast, providing the Ar flow radially or axially did not prevent the back flow of gases below Ar flow rates of 15 L min^{-1}.

Energy Flows—Fig. 8 shows the instantaneous energy balance as a function of time for the reduction stage performed with $P_{solar}=3.8$ kW. Indicated is the heat consumed by the endothermic reaction, the sensible heat content of reactor components, and the heat losses by conduction, convection, and radiation (reflected and re-emitted). Heating of the reactor components (reactor shell, Al_2O_3–SiO_2 insulation, CeO_2 laminate, CeO_2 RPC) consumed 31% of P_{solar} on average, but account for 17% of P_{solar} at the end of reduction ($t=46$ min). Conductive losses to the water-cooled front and through the insulated walls were significant and accounted for 16% of P_{solar} on average. Radiative losses, the dominant source of irreversibility, increased considerably with reduction time due to the increasing cavity temperature and accounted for 48% of P_{solar} on average and 57% of P_{solar} peak. Sensible heat loss by the out-flowing gas (Ar/O_2 mixture) and convection losses at the window and water-cooled surfaces were less significant and amounted to 1% each. The remaining fraction of energy, about
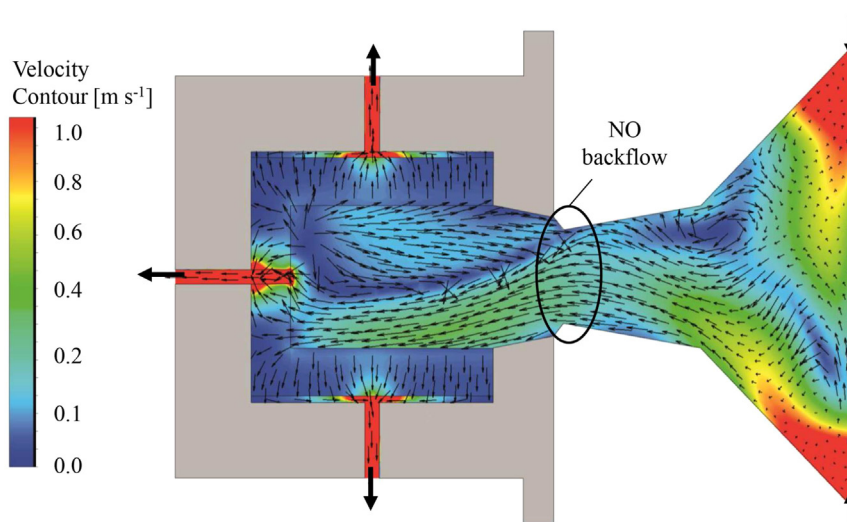
Fig. 7. Velocity contour plot and normalized velocity vectors in the vertical cross-section for a stationary simulation performed at $P_{solar}=2.8$ kW. Argon purge gas is provided tangentially through 6 nozzles at the window circumference and exits the reactor through 4 radial and one axial outlet ports.
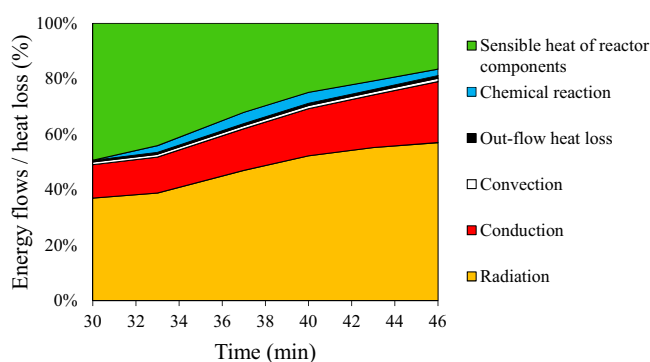
Fig. 8. Instantaneous energy balance based on the numerical model for $P_{solar}=3.8$ kW. Indicated are the heat consumed by the endothermic reaction (Chemical reaction), the sensible heat of the reactor components, and the heat losses by conduction, convection, and radiation (reflected-and re-radiated).

2.9% of P_{solar}, was consumed by the endothermic reduction of CeO_2.

There is room for optimization of the aperture's size to maximize the absorption of P_{solar} and minimize re-radiation losses (Steinfeld and Schubnell, 1993). The cavity's ability to capture P_{solar} is given by the apparent absorptivity, $\alpha_{apparent}$, defined as the fraction of radiative flux across the aperture that is absorbed by the cavity walls. $\alpha_{apparent}$, determined by MC, is only 0.85 because of 10% reflection losses escaping through the aperture and 5% absorption losses on water-cooled surfaces inside the cavity. Selective coatings for quartz windows with high transmissivity in the visible region of the solar spectrum and high surface reflectivity in the IR region around the 1.5 μm (Wien's displacement law for Planck's blackbody radiation at 2000 K) can help recapture some of the reflected and emitted radiation by the hot cavity, provided these coatings withstand the high temperatures (Maag et al., 2011). Energy required for heating the reactor components can be reduced by using thermal insulation materials with lower specific heat capacities. Further, minimizing ΔT between the reduction and oxidation steps of the cyclic process or operation under pressure-swing isothermal conditions (Bader et al., 2013; Hao et al., 2013; Muhich et al., 2013) (not discussed in this study) can eliminate this energy penalty. Conduction losses can be obviously reduced by improving the insulation and by

avoiding the heat bridges created by water-cooled surfaces, but the Al-made CPC and frustum require active cooling because of the exposure to radiative fluxes exceeding 2000 W/m². Alternative cooling fluids (e.g. oil) should be assessed to minimize ΔT between the hot cavity and actively cooled reactor front. Operation under vacuum pressures could further reduce heat losses to the surrounding, reduce usage of purge gas, and achieve lower O_2 partial pressures (Ermanoski et al., 2013). The radiative properties of the ceria RPC, especially the optical thickness, can be optimized for efficient radiative penetration and absorption by adjusting the pore size and porosity (Suter et al., 2014).

To increase $\eta_{solar-to-fuel}$ an alternative solar reactor design depicted in Fig. 9 is proposed. The cavity has a conical shape to enable a more uniform distribution of absorbed incoming radiation and to avoid hot spots. A $\theta_i - \theta_o$ secondary concentrator (Rabl and Winston, 1976) with acceptance angle $\theta_i=45°$ and exit angle $\theta_o=60°$ is incorporated to reduce the aperture diameter to 3.5 cm, boost the solar concentration ratio, and prevent direct high-flux irradiation of the insulation close to the aperture. This element is actively cooled but maintained at $T=573$ K to lower conduction losses. The ceria mass loading is increased to 2500 g to enhance the ratio of reactive to inert material (insulation, shell). Purge and reactant gases are provided tangentially via 6 radially arranged injection nozzles located close to the quartz window. Product gases exit the reactor through four radial and one axial outlet port.

Fig. 10 shows the numerically calculated average temperatures of the ceria RPC, Al_2O_3–SiO_2 insulation, and reactor shell along with the O_2 evolution rate during a redox cycle at $P_{solar}=2.0$ kW. The non-solar oxidation step was modeled assuming a 20 min cooling phase with $P_{solar}=0$ kW. During thermal reduction, an average ceria heating rate of 18.0 K min^{-1} is predicted leading to peak average ceria temperature of 1963 K min^{-1}. Similar to the cylindrical cavity, O_2 evolution starts immediately after increasing P_{solar} and reaches peak and average rates of 0.15 and 0.1155 mL min^{-1} g^{-1} CeO_2, respectively. The total predicted O_2 evolution is 3 times higher than the one experimentally achieved with the cylindrical cavity.

Fig. 11 shows the temperature distribution (a) and the O_2-concentration (b) along with the normalized velocity vectors of the flow field in the vertical cross-section of the solar reactor at the end of the reduction step ($t=40$ min) and at peak O_2 evolution ($t=20$ min) performed at $P_{solar}=2.0$ kW, respectively. The conical cavity design coupled to the $\theta_i - \theta_o$ secondary concentrator results in
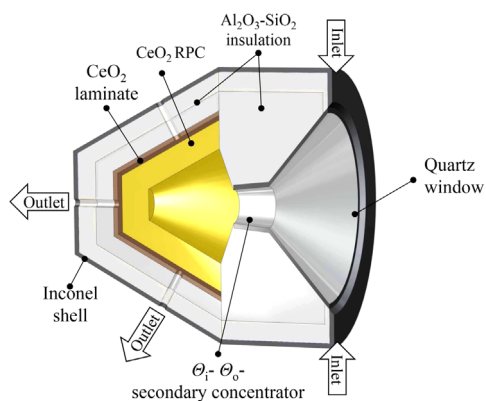
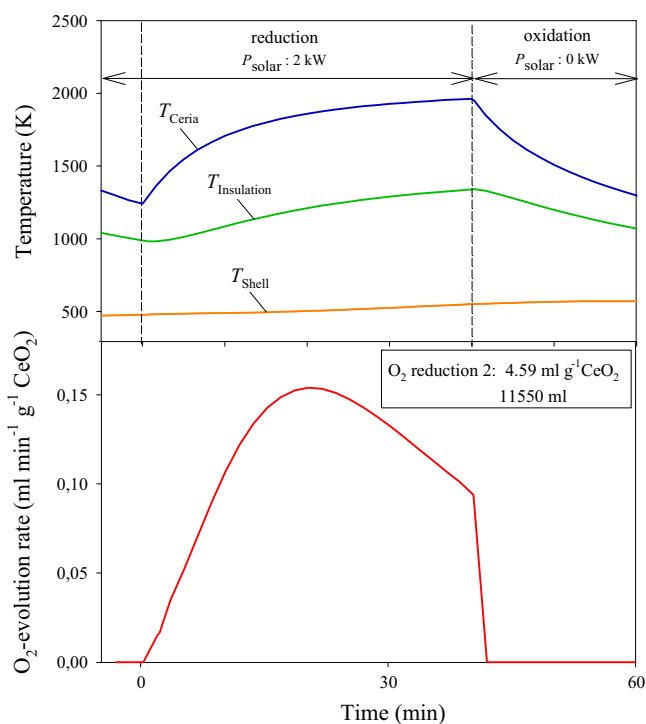**Fig. 9.** Schematic of the conical solar reactor configuration.

Fig. 10. Numerically calculated average temperatures of the ceria RPC, Al_2O_3–SiO_2 insulation, and reactor shell and (bottom) numerically calculated O_2 evolution rate at the reactor outlets for a redox cycles with $P_{solar}=2$ kW during reduction and $P_{solar}=0$ kW during oxidation.
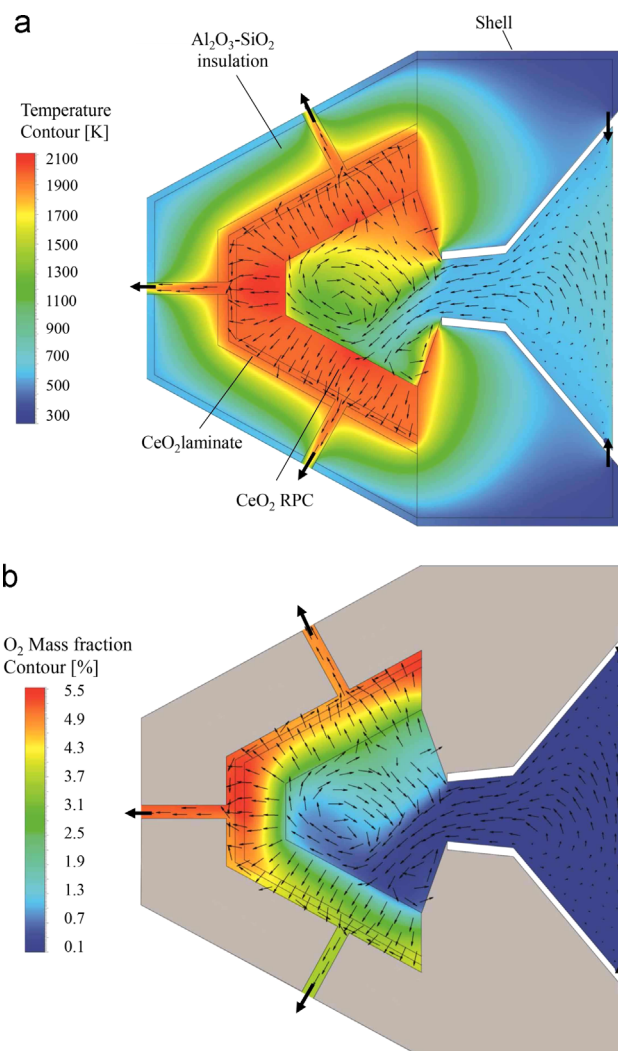

Fig. 11. (a) Normalized velocity vectors and temperature distribution in the vertical cross-section of the cavity-receiver at the end of the reduction step ($t=40$ min) performed with $P_{solar}=2.0$ kW and (b) normalized velocity vectors and O_2-concentration in the vertical cross-section at peak O_2-evolution ($t=20$ min).

a more homogeneous temperature distribution within the RPC, on average 52 K across the structure, and prevents hot spots and melting of the Al_2O_3–SiO_2 insulation. The tangential injection of purge gas close to the window circumference at flow rates ≥ 7 L min^{-1} induces a swirl flow which prevents backflow of gases into the reactor front and thereby CeO_2 depositions on the secondary concentrator, consistent with the results of Fig. 7.

Furthermore, it also hinders O_2 from circulating into the reactor front which enhances purging. This can be seen in Fig. 11(b) which shows a clear difference in O_2 concentration between the reactor front and the reactor cavity. Assuming stoichiometric oxidation with CO_2 ($r_{CO}=2r_{O_2}$), the new solar reactor design reaches $\eta_{solar-to-fuel}=$ 5.4% (without heat recovery).

The superior performance compared to the cylindrical cavity is attributed to lower radiation and conduction losses (on average 57% lower), to a more uniform temperature distribution within the reactor cavity (av. ΔT across RPC: cylindrical reactor $=145$ K, conical

reactor $=52$ K), to more effective purging of O_2 from the cavity by the Ar flow (av. P_{O_2} at peak O_2-evolution: cylindrical reactor $=0.0999$ atm, conical reactor $=0.0185$ atm), and to a higher mass loading of ceria ($m_{cylindrical}=1413$ g, $m_{conical}=2500$ g). Further increase of $\eta_{solar-to-fuel}$ to 6.4% is feasible by recovering the sensible heat of gases and solids during the temperature swing between reduction and oxidation steps.

6. Summary and conclusions

We have presented a dynamic numerical model of a high-temperature solar reactor that couples Monte-Carlo ray-tracing to computational fluid dynamics. Experimental validation of the model was accomplished by comparing temperatures and O_2 evolution rates with experimentally measured data obtained with a 4-kW solar reactor prototype for a set of experimental runs conducted at ETH's high-flux solar simulator facility. Radiation losses due to reflection and re-emission and conduction losses through water-cooled components were identified as the major heat losses, accounting for 48% and 16% of the total solar radiative power input, respectively. Temperature distribution inside the cavity was observed to depend on the distribution

of absorbed incoming radiation and reached peak values of 2250 K at highly exposed regions close to the aperture. Such high temperatures induce ceria sublimation and cause local melting of the Al_2O_3-SiO_2 insulation. Further complication aroused from the buoyancy-driven natural convection flow carrying CeO_2 (g) towards the actively-cooled reactor front where it eventually condensed, thereby reducing the CPC's surface reflectance and consequently the radiative power input through the aperture. Increasing the purge gas flow rate and reversing the flow direction by providing the gas tangentially through 6 nozzles close to the window circumference is found to prevent the backflow of gas to the reactor front.

An alternative reactor design featuring a conical cavity shape coupled to $\theta_i - \theta_o$ secondary concentrator enabled a more uniform distribution of absorbed incoming radiation and prevented hot spots on the insulation. Lower radiation/conduction losses, higher ceria mass loading, and effective purging of evolved O_2 resulted in $\eta_{solar-to-fuel}$ of 5.4% (without heat recovery). Further increase of $\eta_{solar-to-fuel}$ to 6.4% is feasible by recovering the sensible heat of gases and solids during the temperature swing between reduction and oxidation steps. Other improvements include the use of selective coatings for quartz windows, RPC with optimized pore size and porosity, and operation under pressure-swing isothermal conditions.

Nomenclature

Symbols

A_{fs}	fluid–solid area density (m^{-1})
a_i	fitting parameter
b_i	fitting parameter
C	solar concentration ratio
c_p	heat capacity($J\,mol^{-1}\,K^{-1}$)
E_{inert}	energy for inert gas separation from the air ($J\,mol^{-1}$)
h	enthalpy ($J\,kg^{-1}$)
$h_{convection}$	convective heat transfer coefficient ($W\,m^{-2}\,K^{-1}$)
h_{fs}	interphaseal heat transfer coefficient ($W\,m^{-2}\,K^{-1}$)
ΔH_{fuel}	higher heating value of the fuel ($J\,mol^{-1}$)
ΔH	reaction enthalpy ($J\,mol^{-1}$)
I	radiation intensity ($W\,m^{-2}$)
I_b	blackbody radiation emission intensity ($W\,m^{-2}$)
$\overline{\overline{I}}$	identity matrix
$\overline{\overline{K}}$	isotropic porosity tensor
k	thermal conductivity ($W\,m^{-1}\,K^{-1}$)
P_{solar}	radiation power input (W)
p	pressure (atm)
Q_{fs}	fluid–solid heat source (W)
$\overline{r}$	position vector
r_{fuel}	molar fuel production rate ($mol\,s^{-1}$)
r_{O_2}	molar oxygen evolution rate ($mol\,s^{-1}$)
r_{inert}	flow rate of inert gas ($mol\,s^{-1}$)
s	path length (m)
$\overline{s}$	direction vector
S_{C,O_2}	oxygen mass source ($mol\,m^{-3}\,s^{-1}$)
$S_{E,solar}$	radiation source ($W\,m^{-2}/W\,m^{-3}$)
$S_{E,reaction}$	reaction energy source ($W\,m^{-3}$)
$\overline{S}_{M,buoy}$	buoyancy momentum loss vector ($kg\,m\,s^{-1}$)
$\overline{S}_{M,porous}$	porous momentum loss vector ($kg\,m\,s^{-1}$)
T	temperature (K)
T_s	solid temperature (K)
T_f	fluid temperature (K)
ΔT	temperature difference (K)
t	time (s)
$\overline{U}$	velocity vector ($m\,s^{-1}$)
Y_{O_2}	O_2 concentration

Greek symbols

α	absorption coefficient (m^{-1})
$\alpha_{apparent}$	apparent cavity absorptance
β	extinction coefficient (m^{-1})
σ	scattering coefficient (m^{-1})
δ	nonstoichiometry
ε	porosity
ε_s	surface emittance
μ	dynamic viscosity ($kg\,m^{-1}\,s^{-1}$)
ρ	density ($kg\,m^{-3}$)
ρ_s	surface total reflectance
τ_s	transmittance
ω	solid angle (deg)
$\eta_{solar-to-fuel}$	solar-to-fuel energy conversion efficiency
∇q_r	radiation source term (W)

Dimensionless Groups

Br	Birkman number
Pe	Péclet number
Pe_{mass}	Péclet number for mass transport
Pe_{th}	Péclet number for heat trasfer
Re	Reynolds number

Abbreviations

CCD	charge-coupled device
CFD	computational fluid dynamics
CPC	compound parabolic concentrator
ETH	Swiss Federal Institute of Technology
GC	gas chromatography
HFSS	High-Flux Solar Simulator
MC	Monte-Carlo method
RPC	reticulated porous ceramic
SLPM	standard liters per minute at 273.15 K and 1 atm

References

Abanades, S., Flamant, G., 2006. Thermochemical hydrogen production from a two-step solar-driven water-splitting cycle based on cerium oxides. Sol. Energy 80 (12), 1611–1623.

Ansys Inc., 2012. Ansys CFX-Solver Theory Guide, Release 14.5.

Bader, R., Venstrom, L.J., Davidson, J.H., Lipiński, W., 2013. Thermodynamic analysis of isothermal redox cycling of ceria for solar fuel production. Energy Fuels.

Chueh, W.C., Haile, S.M., 2010. A thermochemical study of ceria: exploiting an old material for new modes of energy conversion and CO_2 mitigation. Philos. Transact. A Math. Phys. Eng. Sci. 368 (1923), 3269–3294.

Chueh, W.C., Falter, C., Abbott, M., Scipio, D., Furler, P., Haile, S.M., Steinfeld, A., 2010. High-flux solar-driven thermochemical dissociation of CO_2 and H_2O using nonstoichiometric ceria. Science 330 (6012), 1797–1801.

Chueh, W.C., McDaniel, A.H., Grass, M.E., Hao, Y., Jabeen, N., Liu, Z., Haile, S.M., McCarty, K.F., Bluhm, H., El Gabaly, F., 2012. Highly enhanced concentration and stability of reactive Ce^{3+} on doped CeO_2 surface revealed in operando. Chem. Mater. 24 (10), 1876–1882.

Churchill, S.W., Chu, H.H.S., 1975. Correlating equations for laminar and turbulent free convection from a vertical plate. Int. J. Heat Mass Transf. 18 (11), 1323–1329.

Churchill, S.W., Chu, H.H.S., 1975. Correlating equations for laminar and turbulent free convection from a horizontal cylinder. Int. J. Heat Mass Transf. 18 (9), 1049–1053.

Diver, R.B., Miller, J.E., Allendorf, M.D., Siegel, N.P., Hogan, R.E., 2008. Solar thermochemical water-splitting ferrite-cycle heat engines. J. Sol. Energy Eng. 130 (4), 041001–041008.

Ermanoski, I., Siegel, N.P., Stechel, E.B., 2013. A new reactor concept for efficient solar-thermochemical fuel production. J. Sol. Energy Eng. 135 (3), 2019–2026.

Furler, P., Scheffe, J.R., Gorbar, M., Moes, L., Vogt, U., Steinfeld, A., 2012. Solar thermochemical CO_2 splitting utilizing a reticulated porous ceria redox system. Energy Fuels 26, 7051–7059.

Furler, P., Scheffe, J.R., Steinfeld, A., 2012. Syngas production by simultaneous splitting of H_2O and CO_2 via ceria redox reactions in a high-temperature solar reactor. Energy Environ. Sci. 5 (3), 6098.

Furler, P., Scheffe, J., Marxer, D., Gorbar, M., Bonk, A., Vogt, U., Steinfeld, A., 2014. Thermochemical CO_2 splitting via redox cycling of ceria reticulated foam structures with dual-scale porosities. Phys. Chem. Chem. Phys. 16, 10503–10511.

Haering, H.-W., 2008. The Air Gases Nitrogen, Oxygen and Argon. Wiley-VCH Verlag GmbH.

Hao, Y., Yang, C.-K., Haile, S.M., 2013. High-temperature isothermal chemical cycling for solar-driven fuel production. Phys. Chem. Chem. Phys. 15 (40), 17084–17092.

Haussener, S., Coray, P., Lipinski, W., Wyss, P., Steinfeld, A., 2010. Tomography-based heat and mass transfer characterization of reticulate porous ceramics for high-temperature processing. J. Heat Transf. 132 (2), 023305.

Kaneko, H., Miura, T., Fuse, A., Ishihara, H., Taku, S., Fukuzumi, H., Naganuma, Y., Tamaura, Y., 2007. Rotary-type solar reactor for solar hydrogen production with two-step water splitting process. Energy Fuels 21 (4), 2287–2293.

Kodama, T., Enomoto, S.-i., Hatamachi, T., Gokon, N., 2008. Application of an internally circulating fluidized bed for windowed solar chemical reactor with direct irradiation of reacting particles. J. Sol. Energy Eng. 130 (1), 014504.

Lapp, J., Davidson, J.H., Lipiński, W., 2013. Heat transfer analysis of a solid–solid heat recuperation system for solar-driven nonstoichiometric redox cycles. J. Sol. Energy Eng. 135 (3), 031004.

Lockwood, F.C., Shah, N.G., 1981. A new radiation solution method for incorporation in general combustion prediction procedures. Symp. (Int.) Combust. 18 (1), 1405–1414.

Maag, G., Falter, C., Steinfeld, A., 2011. Temperature of a quartz/sapphire window in a solar cavity-receiver. J. Sol. Energy Eng. 133 (1), 014501.

Miller, J.E., McDaniel, A.H., Allendorf, M.D., 2013. Considerations in the design of materials for solar-driven fuel production using metal-oxide thermochemical cycles. Adv. Energy Mater. 4 (2), 1300469.

Mizuno, M., Berjoan, R., Coutures, J.-P., Foex, M., 1975. Phase diagram of the system Al_2O_3–CeO_2 at liquidus temperature. J. Ceram. Assoc. Jpn. 83 (954), 90–96.

Muhich, C.L., Evanko, B.W., Weston, K.C., Lichty, P., Liang, X., Martinek, J., Musgrave, C.B., Weimer, A.W., 2013. Efficient generation of H_2 by splitting water with an isothermal redox cycle. Science 341 (6145), 540–542.

Panlener, R.J., Blumenthal, R.N., Garnier, J.E., 1975. A thermodynamic study of nonstoichiometric cerium dioxide. J. Phys. Chem. Solids 36 (11), 1213–1222.

Perkins, C., Weimer, A.W., 2004. Likely near-term solar-thermal water splitting technologies. Int. J. Hydrog. Energy 29 (15), 1587–1599.

Petrasch, J., 2010. A free and open source Monte Carlo ray tracing program for concentrating solar energy research. In: Proceedings of the ASME Conference, pp. 125–132.

Petrasch, J., Meier, F., Friess, H., Steinfeld, A., 2008. Tomography based determination of permeability, Dupuit–Forchheimer coefficient, and interfacial heat transfer coefficient in reticulate porous ceramics. Int. J. Heat Fluid Flow 29 (1), 315–326.

Petrasch, J.r., Coray, P., Meier, A., Brack, M., Häberling, P., Wuillemin, D., Steinfeld, A., 2007. A novel 50 kW 11,000 suns high-flux solar simulator based on an array of Xenon arc lamps. J. Sol. Energy Eng. 129 (4), 405.

Rabl, A., Winston, R., 1976. Ideal concentrators for finite sources and restricted exit angles. Appl. Opt. 15 (11), 2880–2883.

Scheffe, J.R., Steinfeld, A., 2012. Thermodynamic analysis of cerium-based oxides for solar thermochemical fuel production. Energy Fuels 26 (3), 1928–1936.

Scheffe, J.R., Welte, M., Steinfeld, A., 2014. Thermal reduction of ceria within an aerosol reactor for H_2O and CO_2 splitting. Ind. Eng. Chem. Res. 53 (6), 2175–2182.

Seguin, D., Montillet, A., Comiti, J., Huet, F., 1998. Experimental characterization of flow regimes in various porous media—II: transition to turbulent regime. Chem. Eng. Sci., 53; , pp. 3897–3909.

Siegel, R., Howell, J., 2002. Thermal Radiation Heat Transfer. Taylor&Francis.

Smestad, G.P., Steinfeld, A., 2012. Review: photochemical and thermochemical production of solar fuels from H_2O and CO_2 using metal oxide catalysts. Ind. Eng. Chem. Res. 51, 11828–11840.

Special Metal Corporation. 2014, Physical Constants and Thermal Properties Inconel 600. ⟨http://www.specialmetals.com/documents/Inconel⟩ alloy 600 (Sept 2008).pdf, January 2014.

Steinfeld, A., 2005. Solar thermochemical production of hydrogen––a review. Sol. Energy 78 (5), 603–615.

Steinfeld, A., Schubnell, M., 1993. Optimum aperture size and operating temperature of a solar cavity-receiver. Sol. Energy 50 (1), 19–25.

Suter, S., Steinfeld, A., Haussener, S., 2014. Pore-level engineering of macroporous media for increased performance of solar-driven thermochemical fuel processing. Int. J. Heat Mass Transf. 78 (0), 688–698.

Touloukian, Y., 1967. Thermophysical properties of high temperature solid materials: oxides and their solutions and mixtures. Part I: simple oxygen compunds and theire mixtures. Thermophysical Properties Research Center, Purdue University.

Touloukian, Y., Dewitt, D., 1972. Thermal Radiative Properties Nonmetallic Solids. Vol. 8. IFI/Plenum, New York, Washington.

Welford, W.T., Winston, R., 1989. High Collection Nonimaging OpticsAcademic Press, San Diego.

Zimmermann, D., 2012. Flow Modeling of a Solar Thermogravimeter Master thesis. ETH Zurich, Switzerland.

Zinkevich, M., Djurovic, D., Aldinger, F., 2006. Thermodynamic modelling of the cerium–oxygen system. Solid State Ion. 177 (11-12), 989–1001.

Zircar Zirconia, 2014. Aluminium Boards, Discs & Cylinders, TYPE Buster. ⟨http://www.zircarzirconia.com/doc/GA-B.pdf⟩, January 2014.

Zircar Zirconia, Inc., 2014. Thermal Conductivity of Zircar Zirconia Fibrous Insulation. ⟨http://zircarzirconia.com/technical-documents/thermal-conductivity-zircar-zirconia-fibrous-insulation/⟩, January 2014.